

Data-Driven Calibration Technique for Quantitative Radar Imaging

Zacharie Idriss and Raghu G. Raj
U.S. Naval Research Laboratory, Washington DC

Abstract—Quantitative inversion algorithms allow for the reconstruction of electrical properties (such as permittivity and conductivity) for every point in a scene. However, such techniques are challenging to use on measured backscattered phase history signals and datasets due to the need to know the incident wave field in the scene. In general, this is unknown due to factors such as antenna characteristics, path loss, waveform factors, etc. In this paper, we introduce a scalar calibration factor to account for these factors. To solve for the calibration factor, we augment the inversion procedure by including the forward problem, which we solve by training a simple feed-forward fully connected neural network to learn a mapping between the underlying permittivity distribution and the scattered field at the radar. We then minimize the mismatch between the measured and simulated fields to optimize the scalar calibration factor for each transmitter. We demonstrate the effectiveness of our data-driven calibration approach on the Fresnel Institute dataset wherein we show the accuracy of the estimated scene permittivities. Our paper thus lays the groundwork for the application of quantitative inversion algorithm in real-world imaging scenarios.

Index Terms—Inverse scattering, quantitative calibration, contrast source inversion, multi-frequency subspace based optimization method

I. INTRODUCTION

In this paper, we present a data-driven calibration technique for quantitative inversion, in particular radar imaging, algorithms. Specifically, we focus on a contrast-source inversion-based quantitative inversion algorithm called the multiple frequency subspace based optimization method (MFSOM) recently developed by the authors [1]. MFSOM reconstructs the electrical properties (e.g., permittivity) of underlying dielectric scatterers. This can augment scatterer identification algorithms in radar imaging applications, by differentiating materials based on permittivity estimates [2], [3]. Quantitative imaging algorithms such as MFSOM first estimate the induced current density by inverting the scattered wave vector within the domain of interest, and second estimate the permittivity from the current estimate, which requires knowledge of the incident field vector. This makes permittivity estimation challenging as there are two equations; one relating the scattered field to the induced current and one relating the induced current to the permittivity; and three unknowns: the induced current, the permittivity, and the incident field. Overcoming this underdetermined system of data driven calibration is paramount for enabling the application of quantitative imaging algorithms to practical radar imaging scenarios.

The most well-known, automatic, data-driven calibration technique for radar imaging was developed by researchers

at the University of Manitoba, which involves solving the forward problem to find a set of weights to apply to the rest of the dataset [4]. This technique requires prior knowledge about the scene structure in order to determine the data calibration strategy [5]. Another set of techniques is rooted in the source reconstruction method, which relies on knowing the total and scattered field at the receiver to find an equivalent current model at the transmitter of the incident field, thus alleviating the need for calibration [6]–[8]. Some techniques involve simply knowing the total field [9]–[12]. Data-driven techniques include introducing scaling factors on the incident wave-field and simultaneously solving for them along with the remaining quantities [13]–[15]. Data-driven techniques using machine learning [16], [17] and compressive sensing [18] approaches have also been recently explored in the literature.

In this paper, we augment the original inverse problem by adding a third objective into the underlying cost function; the error between the simulated and scattered wave fields—such that the simulated fields are generated by executing the forward problem. The forward problem involves predicting the electromagnetic fields based on a known model of the medium’s properties (e.g., permittivity and conductivity distributions). The simulated wave field is found at each iteration by passing the current contrast function to the forward problem and solving for the scattered wave field. We introduce a calibration factor, λ_c , that weights both the simulated scattered wave field and the incident field within the state equation. We then use the conjugate gradient descent (CGD) algorithm to find the optimal calibration factor at each iteration. We show that because the incident field is linearly proportional to the scattered field, we can pull out the calibration factor and use it to weight the incident field.

Naturally, solving the forward problem at each iteration is computationally expensive. To overcome this, we train a simple feed-forward, fully-connected, neural network (FCNN) to learn a forward operator between the scene and the scattered wave field. Using this pre-trained network, we introduce the forward problem in our inverse algorithm without any significant computational cost. We observe that by training the FCNN using a variety of examples, we are able to overcome the need to solve the forward problem in an exact manner. We demonstrate the effectiveness of our data-driven quantitative imaging algorithm using the Fresnel Institute dataset [19].

In our equations, uppercase symbols denote operators or large-scale functions (e.g. \mathcal{M}), while lowercase symbols represent physical fields or parameters at a specific point (e.g., \mathbf{r} for position). Boldface symbols (e.g., \mathbf{E} and \mathbf{W}) indicate

matrix representations of vector fields, while non-bold symbols represent either scalar quantities (e.g., ω for angular frequency and χ for a scalar field) or vector fields (e.g. \mathcal{E} and \mathcal{W}).

II. FORWARD PROBLEM

We start with the Lippmann–Schwinger equation for the total electric field [20] $\mathcal{E}(\mathbf{r}):\mathbb{R}^2 \rightarrow \mathbb{C}$ in volts per meter (V/m),

$$\mathcal{E}(\mathbf{r}) = \mathcal{E}_{\text{inc}}(\mathbf{r}) + j\omega\mu \int_V \mathbf{g}(\mathbf{r}, \mathbf{r}') \mathcal{W} d\mathbf{r}', \quad (1)$$

where $\mathcal{E}_{\text{inc}}(\mathbf{r}):\mathbb{R}^2 \rightarrow \mathbb{C}$ is the incident electric field in V/m, V is the region of integration in cubic meters (m^3), $\mathbf{g}(\mathbf{r}, \mathbf{r}'):\mathbb{R}^2 \times \mathbb{R}^2 \rightarrow \mathbb{C}$ is the Green's function in meters (m), and $\mathcal{W}(\mathbf{r}'):\mathbb{R}^2 \rightarrow \mathbb{C}$ is the current density in amperes per square meter (A/m^2). In general, (1) is expressed in matrix form as:

$$\mathbf{E} = \mathbf{E}_{\text{inc}} + \mathbf{G}\mathbf{W}, \quad (2)$$

where, \mathbf{E} , \mathbf{E}_{inc} , \mathbf{G} , and \mathbf{W} are the matrix representations of \mathcal{E} , \mathcal{E}_{inc} , \mathbf{g} , and \mathcal{W} respectively, which are determined through the Method of Moments using a pulse basis function expansion and point collocation (Dirac delta distributions) [21]. From (1) and using the constitutive relations for linear isotropic media [22], we define a linear operator $\mathcal{M}:\mathbf{W} \rightarrow \mathbf{E}_{\text{inc}}$ as

$$\mathcal{M}[\mathcal{W}](\mathbf{r}) = \frac{\mathcal{W}(\mathbf{r})}{i\omega\epsilon_0\chi(\mathbf{r})} - j\omega\mu \int_V \mathbf{g}(\mathbf{r}, \mathbf{r}') \mathcal{W}(\mathbf{r}') d\mathbf{r}' \quad (3)$$

where ω is the angular frequency in radians per second (rad/s), ϵ_0 is the permittivity of free space in farads per meter (F/m), and $\chi(\mathbf{r}):\mathbb{R}^2 \rightarrow \mathbb{C}$ is the susceptibility, a dimensionless parameter.

Then, expressing (3) with $\lambda_c \in \mathbb{C}$, the unknown calibration factor to be determined, we have,

$$\mathcal{M}[\mathcal{W}](\mathbf{r}) = \lambda_c \mathcal{E}_{\text{inc}}(\mathbf{r}). \quad (4)$$

Solving for $\mathcal{W}(\mathbf{r})$ explicitly, we obtain:

$$\mathcal{W}(\mathbf{r}) = \lambda_c \mathcal{M}^{-1} \mathcal{E}_{\text{inc}}(\mathbf{r}),$$

showing the current density $\mathcal{W}(\mathbf{r})$ in terms of the inverse of the operator \mathcal{M} applied to the scaled incident field $\lambda_c \mathcal{E}_{\text{inc}}(\mathbf{r})$. Thus, the scattered field is expressed, using Green's Theorem, as

$$\mathcal{E}_{\text{scat}}(\mathbf{r}_{\text{rec}}) = \lambda_c \int_V \mathbf{g}(\mathbf{r}_{\text{rec}}, \mathbf{r}') \mathcal{M}^{-1} \mathcal{E}_{\text{inc}}(\mathbf{r}') d\mathbf{r}'. \quad (5)$$

Equation (5) is expressed in matrix form as:

$$\mathbf{E}_s = \lambda_c \mathbf{G}\mathbf{W}, \quad (6)$$

where \mathbf{E}_s is the matrix representation of $\mathcal{E}_{\text{scat}}$.

III. DATA-DRIVEN CALIBRATION

In the MFSOM algorithm [1], the current is separated into distinct subspaces—a signal and a noise subspace—using the singular value decomposition (SVD) of the Green's functions as

$$\mathbf{G} = \mathbf{U}\mathbf{\Sigma}\mathbf{V}^*$$

where the matrices \mathbf{U} , $\mathbf{\Sigma}$, and \mathbf{V} denote the left singular vectors, singular values, and right singular vectors, respectively. Using this formulation, the cost function is presented as

$$J(\mathbf{W}, \chi) = \sum_{p=1}^P \left(\frac{\|\mathbf{E}_s^p - \mathbf{G}\mathbf{W}^p\|_2^2}{\|\mathbf{E}_s^p\|_2^2} + \frac{\|\mathbf{W}^p - \chi(\mathbf{E}_{\text{inc}}^p + \mathbf{E}_d^p)\|_2^2}{\|\mathbf{W}_+^p\|_2^2} \right) \quad (7)$$

where \mathbf{E}_s^p denotes the measured scattered field for the p -th incident field, \mathbf{E}_d^p denotes the scattered field within the domain of interest (i.e., when both \mathbf{r}, \mathbf{r}' in (5) denote points in the scene), \mathbf{G} is Green's function, the dominant current subspace is defined as

$$\mathbf{W}_+^p = \mathbf{V}_+^p \mathbf{w}_+^p, \quad \mathbf{w}_+^p = \frac{\mathbf{U}_+^* \mathbf{E}_s^p}{\mathbf{\Sigma}_+}$$

for the p -th incident field, the subscript $+$ denotes the signal subspace, and $\mathbf{E}_{\text{inc}}^p$ is the incident field for the p -th source. We further remark that the first term in equation (7) is called the data-fidelity term, whereas the second term in (7) is called the state equation mismatch term.

As seen from (7), the incident field in the state equation mismatch is scaled by the scalar field, χ . However, in received backscattered signals or measured datasets, the incident field is scaled by unknown factors such as antenna beam pattern, antenna gain, and waveform amplitudes, which have to be estimated to accurately reconstruct χ . To account for all these effects, we optimize for the scalar calibration factor (for each calibration angle), λ_c^p , and augment the problem (7) as

$$J(\mathbf{W}, \chi, \{\lambda_c\}_{p=1}^P) = \sum_{p=1}^P \left(\frac{\|\mathbf{E}_s^{\text{meas},p} - \mathbf{G}\mathbf{W}^p\|_2^2}{\|\mathbf{E}_s^{\text{meas},p}\|_2^2} + \frac{\|\mathbf{W}^p - \chi(\lambda_c^p \mathbf{E}_{\text{inc}}^p + \mathbf{E}_d^p)\|_2^2}{\|\mathbf{W}_+^p\|_2^2} + \frac{\|\lambda_c^p \mathbf{E}_s^{\text{sim},p} - \mathbf{E}_s^{\text{meas},p}\|_2^2}{\|\mathbf{E}_s^{\text{meas},p}\|_2^2} + \beta |\lambda_c^p|^2 \right) \quad (8)$$

where $\mathbf{E}_s^{\text{sim}}$ represents the simulated field vector, $\mathbf{E}_s^{\text{meas}}$ is the measured field vector, and $\beta \in \mathbb{R}$ is the regularization parameter balancing data fidelity and smoothness. As shown in (5), the added calibration factor that scales the incident field in the forward operator is factored out as \mathcal{M} is a linear operator. Thus, minimizing the third term in (8) with respect to λ_c provides the correct scaling, used to scale the incident field in the second term in (8).

In (8), $\mathbf{E}_s^{\text{sim}}$ is found by first solving (4), which can be computationally expensive for a large domain, high dielectric constant, or large number of frequencies. Therefore, as detailed in Subsection III-A, we train an FCNN to learn a mapping (shown in Fig. 1) that enables us to solve for the scattered field much faster once the FCNN is trained. Importantly, the central benefit of this approach is that the resulting algorithm can be applied to a received backscattered signal without the need for knowing the scene structure in advance.

To find the optimal $\lambda_c \in \mathbb{C}$ that minimizes the error between the measured and simulated fields, we define the objective as

$$\{\lambda_c\}_{p=1}^P = \arg \min_{\{\lambda_c\}_{p=1}^P \in \mathbb{C}} J(\mathbf{W}, \chi, \{\lambda_c\}_{p=1}^P).$$

CGD is used to solve for λ_c , where search directions are found using the gradient $g = \nabla_{\lambda_c} J$ to inform an *adaptive* search direction, d , using the Polak–Ribiere update [23]. Then, λ_c is found in an iterative manner using the following update rule

$$\lambda_c^{p,(k+1)} = \lambda_c^{p,(k)} + \alpha^{p,(k)} d^{p,(k)}$$

where $\alpha^{p,(k)} \in \mathbb{C}$ is the step size that minimizes the cost function along $d^{p,(k)} \in \mathbb{C}$, and is found using line search minimization. Thus, at each iteration, k , the sub objective of finding the step size, α , is to minimize the cost function

$$\alpha^{p,(k)} = \arg \min_{\alpha \in \mathbb{C}} J(\mathbf{W}, \chi, \lambda_c^{p,(k)} + \alpha d^{p,(k)})$$

along, $d^{p,(k)}$. This objective is minimized by differentiating with respect to α and solving for the optimal $\alpha^{p,(k)}$ in closed form. The pseudo-code of the resulting Quantitative Radar Imaging (QRI) algorithm that incorporates the above steps is presented in Algorithm 1. Thereafter, sub-section III-A details the construction of the neural network used in Algorithm 1 for automatic, data-driven calibration and section IV details the numerical results of the QRI algorithm. In Algorithm 1, T denotes the termination tolerance, and for every result in this paper, it was set to $T = 5 \times 10^{-4}$.

Algorithm 1 QRI with Data-driven Calibration

Input: Define $\mathbf{W}_0, \chi_0, \beta, \{\lambda_{c,0}\}_{p=1}^P = 1, n = 1$
Initialize: $J_{\text{prev}} \leftarrow \infty$ \triangleright Set initial cost function value
while $|J(\mathbf{W}, \chi, \lambda_c) - J_{\text{prev}}| > T$ **do** \triangleright Termination criterion
 $J_{\text{prev}} \leftarrow J(\mathbf{W}, \chi, \{\lambda_c\}_{p=1}^P)$
 $\mathbf{W}_n \leftarrow \arg \min_{\mathbf{W}} J(\mathbf{W}, \chi, \{\lambda_c\}_{p=1}^P)$ \triangleright Induced current
Solve using CGD
 $\chi_n \leftarrow \arg \min_{\chi} J(\mathbf{W}, \chi, \{\lambda_c\}_{p=1}^P)$ \triangleright Contrast function
Solve using CGD
Update $\mathbf{E}_s^{\text{sim}}(\chi_n)$ \triangleright Update simulated field
Using exact forward problem or trained FCNN
 $\{\lambda_{c,n}\}_{p=1}^P \leftarrow \arg \min_{\lambda_c} J(\mathbf{W}, \chi, \{\lambda_c\}_{p=1}^P)$ \triangleright Scaling parameter
Solve using CGD
 $n = n + 1$ \triangleright Update iteration count
end while
Output: Optimized values of $\mathbf{W}, \chi, \{\lambda_c\}_{p=1}^P$

A. Approximate Forward Problem using Neural Network

We train a neural network to learn an arbitrary mapping, \mathcal{F} , as shown in Fig. 1, from the estimated permittivity distribution, $\epsilon_R(\mathbf{r}) \in \mathbb{R}$, to the scattered wave field at the

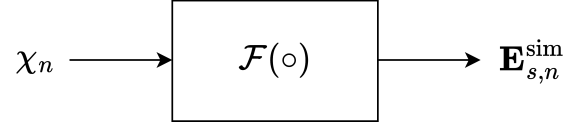


Fig. 1: Flow map for input-output relationship used to train the FCNN. Input: estimated χ . Output: simulated wave field $\mathbf{E}_s^{\text{sim}}$. The subscript n is used to show that this occurs at every iteration of the algorithm.

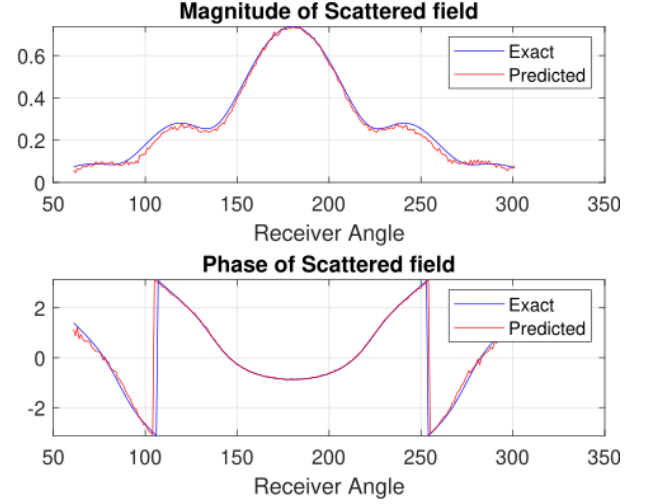


Fig. 2: Predicted versus measured wave field $\mathbf{E}_s^{\text{meas}}$, for the scene in Fig. 3b using the pretrained FCNN. Single transmitter at 0 degrees.

receiver, $\mathbf{E}_s^{\text{sim}}(\mathbf{r}) \in \mathbb{C}$. The mapping from the estimated χ $\mathbf{E}_s^{\text{sim}}$ is expressed as

$$\mathcal{F} : \chi \rightarrow \mathbf{E}_s^{\text{sim}},$$

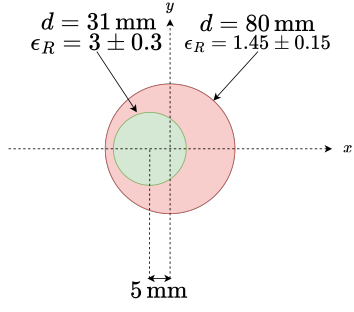
where \mathcal{F} denotes the forward operator that generates $\mathbf{E}_s^{\text{sim}}$ from a given χ .

To construct an optimal neural network with training data, the forward problem was run 100 times for each scattering configuration shown in Fig. 3. Diversity in the training samples was introduced by placing a uniform distribution over the permittivity and assigning each homogeneous scatterer a value chosen as $\epsilon_R \sim \text{Uniform}(1.1, 5)$, where Uniform denotes the uniform distribution. A lower bound was placed on ϵ_R at 1.1 to ensure that each scatterer was sufficiently differentiated from the background and not smaller than unity (which corresponds to the relative permittivity of free space).

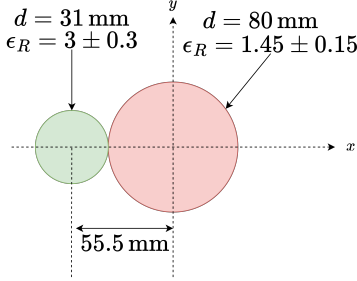
In Fig. 2 we show that using the pre-trained FCNN for the exact scene shown in Fig. 3b, we are able to achieve agreement between the exact and predicted wave fields with a mean square error of $\sim 8.4 \times 10^{-4}$.

IV. NUMERICAL RESULTS

We test our calibration algorithm on the configurations shown in Fig. 3. The configuration in Fig. 3a consists of two dielectric scatterers: the red foam with a relative permittivity of $\epsilon_R = 1.45 \pm 0.15$ and the green plastic with a relative



(a) ‘FoamDielInt’: a foam cylinder (red) with a plastic cylinder (berylon) (green) within it.



(b) ‘FoamDielExt’: a foam cylinder (red) with an external plastic cylinder (berylon) (green).

Fig. 3: Experimental scattering configurations from the Institute Fresnel dataset [19]. In Figs. 3a and 3b, d denotes diameter, and ϵ_R denotes relative permittivity.

permittivity of $\epsilon_R = 3 \pm 0.3$. The configuration in Fig. 3b features the plastic tube now adjacent to the red foam scatterer.

We place a metric on the reconstruction performance of our calibration algorithm using the normalized squared error (NSE) defined as

$$\Delta = \sum_{l=1}^L \frac{|\hat{\epsilon}_l - \epsilon_l|^2}{|\epsilon_l|^2} \quad (9)$$

where $\hat{\epsilon}_l$ denotes the estimated permittivity at pixel l , ϵ_l represents the ground truth value at pixel l , and L is the total number of image pixels.

We first assign a ground truth (GT) calibration factor as $\lambda_c^p = \lambda_c = 2$ i.e., each transmitter is the same, and consider the configuration shown in Fig. 3b. Here, $p = 1, \dots, 8$. We then use the procedure shown in Algorithm 1 to estimate the calibration factor from $\mathbf{E}_s^{\text{meas}}$, at each receiver, together with the induced current, and estimated χ . To present the results of our algorithm, we show the estimated scalar calibration factor in Fig. 4 as a function of iterations, n , to demonstrate convergence of our estimate to the GT value along with the overall cost function shown computed as (8).

Since $\lambda_c^p = \lambda_c = 2$, a single calibration factor is jointly estimated as a function of all p by coherently summing the gradient and step size across p . This approach yields good results when the underlying assumption holds. However, as discussed in Subsection IV-A, this assumption is invalid when

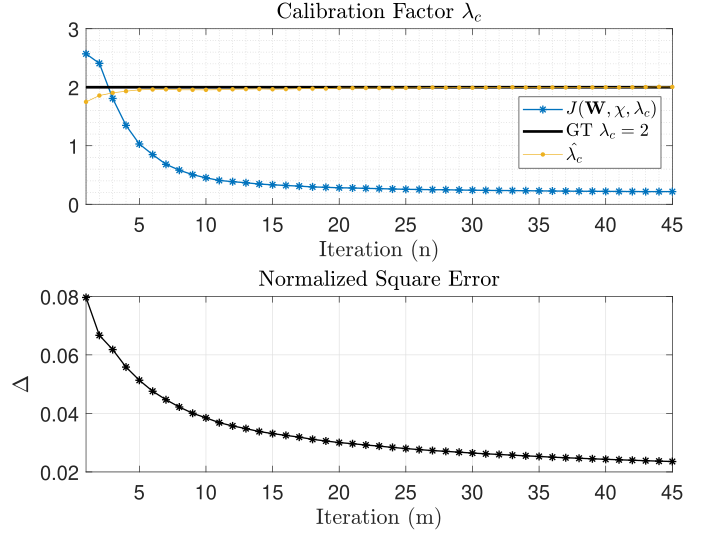


Fig. 4: Jointly estimated calibration factor for all transmitters $p, p = 1, \dots, 8$. *Top*: The cost function value is shown in blue, and the GT value of $\lambda_c = 2$ is shown in black. The yellow line corresponds to the joint estimation of λ_c for all transmitters. The regularization parameter is set to $\beta = 1 \times 10^{-3}$. *Bottom*: NSE where Δ denotes the normalized squared error and is defined in (9).

processing experimental datasets due to unknown channel effects at each angle, which are absent in simulations.

The estimated calibration factor, denoted as $\hat{\lambda}_c$, is shown in Fig. 4 using a yellow line with circle markers. The convergence of the cost function, $J(\mathbf{W}, \chi, \lambda_c)$, is shown in blue with asterisk markers. The GT value for λ_c is shown in black. We show that the data-driven estimation of the calibration factor approaches the GT value. To estimate λ_c in Fig. 4, we use $\beta = 1 \times 10^{-3}$. However, the results depend on a good choice for β , which regularizes the estimation of λ_c as shown in (8), and Algorithm 1. Determining the optimal value of β automatically, is not straightforward, and the choice significantly affects the fidelity of the results.

We now consider the case for a GT value of $\lambda_c^p = \lambda_c = 10$ i.e., each transmitter is the same. The results are shown in Fig. 5 with $\beta = 1 \times 10^{-5}$, where the *top* figure shows the convergence of the cost function in blue, the GT λ_c is shown in black, and $\hat{\lambda}_c$, is shown in yellow.

A. Experimental Dataset

We now test our calibration algorithm on the dataset obtained from the Fresnel Institute [19]. We consider the scattered wave field data corresponding to the scattering configuration shown in Fig. 3b. The dataset consists of $P = 8$ transmitters (Tx) and $Q = 241$ receivers, all located at an equal distance of 1.67 meters from the scene center, located at (0,0) in Fig. 6b.

Fig. 6 shows the results of applying our calibration to the measured data corresponding to Fig. 3b. Fig. 6a shows the absolute values of the calibration factors for Tx₁ to Tx₈ in colored lines with circle markers (note that some of the colored

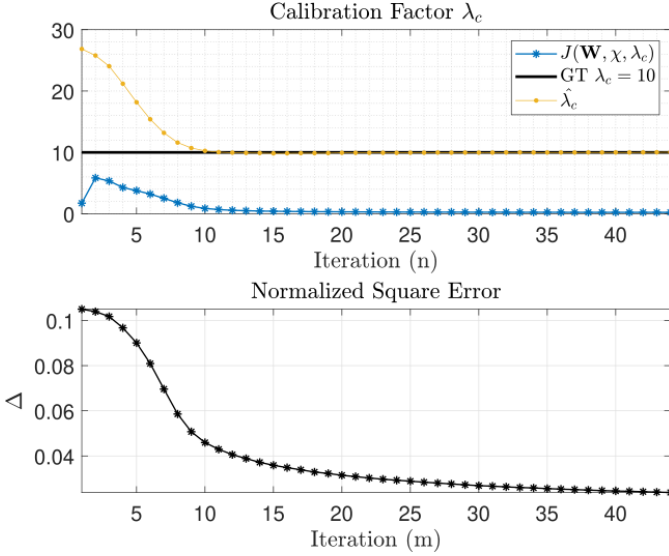


Fig. 5: Jointly estimated calibration factor for all transmitters $p, p = 1, \dots, 8$. *Top*: The cost function value is shown in blue, and the GT value of $\lambda_c = 10$ is shown in black. The yellow line corresponds to the joint estimation of λ_c for all transmitters. The regularization parameter is set to $\beta = 1 \times 10^{-5}$. *Bottom*: NSE where Δ denotes the normalized squared error and is defined in (9).

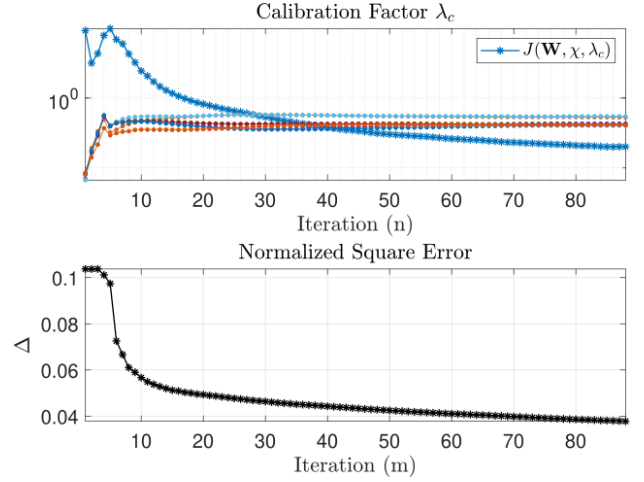
TABLE I: RECONSTRUCTION ERROR

Calibrated	Yes	No
NSE (Δ)	0.038	0.201

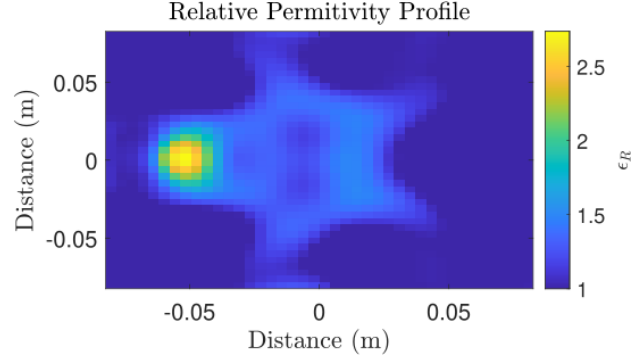
lines obscure each other and are not all visible), and the value of the cost function in (8) for each iteration, n , in blue with asterisk markers. We allow the scalar calibration factor for each Tx to be complex to account for phase factors and find that a purely real calibration factor does not yield a good NSE. Moreover, as can be seen from Fig. 6a, we do not assume $\lambda_c^p = \lambda_c$, and when we test this, the joint estimation yields inferior results. Therefore, it is noted that the assumption that each transmitter is the same does not always hold and that the more general form of the algorithm should be used when such a prior assumption cannot be made. Correspondingly, we present the resulting scene in Fig. 6b, where the color bar on the right-hand side indicates the permittivity value for each pixel. Table I displays the NSE for the reconstruction performance and compares our calibration Algorithm 1 to the NSE when not calibrating the dataset. In Table I, the title *Yes* denotes that the calibration Algorithm 1 was used, and the title *No* denotes that $\lambda_c = 1 \forall p$, i.e. the calibration factor was forced to 1 at each iteration. This result demonstrates the effectiveness and potential of the QRI algorithm for performing accurate quantitative radar imaging on measured datasets in a data-driven way.

V. CONCLUSION

We find that our data-driven calibration technique is able to estimate a scalar calibration factor for each transmitter by incorporating the forward problem into the inverse problem.



(a) *Top*: The estimated calibration factors, λ_c , for the measured dataset (Fig. 3b) from [19] for Tx₁ to Tx₈, are presented on a logarithmic scale. The overall cost function is shown in blue. Here, $\beta = 1$. *Bottom*: NSE where Δ denotes the normalized squared error and is defined in (9).



(b) The corresponding permittivity distribution for the calibration in Fig. 6a. The NSE is 0.038.

Fig. 6: Estimated calibration factors and reconstructed permittivity distribution for the scattering configuration in Fig. 3b.

Since this is computationally expensive, we use an FCNN to avoid having to solve the forward problem exactly at each iteration. We note that adding the forward problem can provide a robust solution to estimating the incident field. An important future challenge arising from this paper is the need to alleviate the dependence of our current QRI algorithm on choosing the right β . This can be realized by automatically adapting β within a neural network processing framework. The resulting algorithm should find wide-ranging applications in quantitative radar imaging including, for example, applications to ground-penetrating radar imaging for estimating the permittivity of the ground and scatterers.

REFERENCES

- [1] Z. Idriss and R. G. Raj, "A multi-frequency quantitative inversion technique for imaging through obscuring media," in *2024 IEEE Conference on Computational Imaging Using Synthetic Apertures (CISA)*, Boulder, CO, USA, 2024, pp. 01–05.
- [2] —, "A physics-based imaging and feature extraction technique for bistatic radar imaging," in *2024 IEEE Conference on Computational Imaging Using Synthetic Apertures (CISA)*, Boulder, CO, USA, 2024, pp. 1–6.

- [3] Z. Idriss, R. G. Raj, and R. M. Narayanan, "A computational electromagnetics and sparsity-based feature extraction approach to ground-penetrating radar imaging," *IEEE Transactions on Geoscience and Remote Sensing*, vol. 60, pp. 1–15, Mar. 2022.
- [4] C. Gilmore, A. Zakaria, P. Mojabi, M. Ostadrahimi, S. Pistorius, and J. L. Vetri, "The university of manitoba microwave imaging repository: A two-dimensional microwave scattering database for testing inversion and calibration algorithms [measurements corner]," *IEEE Antennas and Propagation Magazine*, vol. 53, no. 5, pp. 126–133, 2011.
- [5] R. F. Bloemenkamp, A. Abubakar, and P. M. van den Berg, "Inversion of experimental multi-frequency data using the contrast source inversion method," *Inverse Problems*, vol. 17, no. 6, p. 1611, 2001.
- [6] T. K. Sarkar and A. Taaghoul, "Near-field to near/far-field transformation for arbitrary near-field geometry utilizing an equivalent electric current and MoM," *IEEE Transactions on Antennas and Propagation*, vol. 47, no. 3, pp. 566–573, Mar. 1999.
- [7] F. Qin, "An improved super resolution reconstruction method based on initial value estimation," in *2010 3rd International Congress on Image and Signal Processing*, vol. 2, Yantai, China, 2010, pp. 826–829.
- [8] C. Narendra, I. Jeffrey, and P. Mojabi, "Using the source reconstruction method to model incident fields in microwave tomography," *IEEE Antennas and Wireless Propagation Letters*, vol. 16, pp. 46–49, 2017.
- [9] K. Sastry, C. Bhat, R. Solimene, and U. K. Khankhoje, "Electromagnetic field imaging in arbitrary scattering environments," *IEEE Transactions on Computational Imaging*, vol. 7, pp. 224–233, 2021.
- [10] R. Yang, Z. Q. Meng, and T. Takenaka, "Extraction of incident field from total field data," in *2016 Progress in Electromagnetic Research Symposium (PIERS)*, Shanghai, China, 2016, pp. 4073–4077.
- [11] T. Tsuburaya, Z. Meng, and T. Takenaka, "Inverse scattering analysis from measurement data of total electric and magnetic fields by means of cylindrical-wave expansion," *Electronics*, vol. 8, no. 4, p. 417, 2019. [Online]. Available: <https://www.mdpi.com/2079-9292/8/4/417>
- [12] R. Yang, Z. Q. Meng, and T. Takenaka, "Conjugate gradient method applied to inverse scattering with no prior information on incident field," in *2017 Progress in Electromagnetics Research Symposium - Fall (PIERS - FALL)*, Singapore, 2017, pp. 731–736.
- [13] Y. Chang and Y. Guo, "An optimization method for the inverse scattering problem of the biharmonic wave," *Communications on Analysis and Computation*, vol. 1, no. 2, pp. 168–182, May 2023.
- [14] S. Nounouh, C. Eyraud, A. Litman, and H. Tortel, "Quantitative imaging with incident field modeling from multistatic measurements on line segments," *IEEE Antennas and Wireless Propagation Letters*, vol. 14, pp. 253–256, 2015.
- [15] E. Kim, C. T. Mohammadi, M. Asefi, J. Lovetri, I. Jeffrey, and C. Gilmore, "Imaging and calibration of electromagnetic inversion data with a single data set," *IEEE Open Journal of Antennas and Propagation*, vol. 3, pp. 12–23, 2022.
- [16] R. Guo, Z. Jia, X. Song, M. Li, F. Yang, S. Xu, and A. Abubakar, "Pixel- and model-based microwave inversion with supervised descent method for dielectric targets," *IEEE Transactions on Antennas and Propagation*, vol. 68, no. 12, pp. 8114–8126, Dec. 2020.
- [17] S. K. Shastri, Y. Ma, P. Boufounos, and H. Mansour, "Deep calibration and operator learning for ground penetrating radar imaging," in *2024 32nd European Signal Processing Conference (EUSIPCO)*, Lyon, France, 2024, pp. 1796–1800.
- [18] A. C. M. Austin and M. J. Neve, "Efficient field reconstruction using compressive sensing," *IEEE Transactions on Antennas and Propagation*, vol. 66, no. 3, pp. 1624–1627, Mar. 2018.
- [19] J.-M. Geffrin, P. Sabouroux, and C. Eyraud, "Free space experimental scattering database continuation: Experimental set-up and measurement precision," *Inverse Problems*, vol. 21, no. 6, p. S117, 2005. [Online]. Available: <https://dx.doi.org/10.1088/0266-5611/21/6/S09>
- [20] X. Chen, *Computational Methods for Electromagnetic Inverse Scattering*. Hoboken, NJ, USA: Wiley-IEEE Press, 2018. [Online]. Available: <https://ieeexplore.ieee.org/book/8371439>
- [21] R. F. Harrington, *Field Computation by Moment Methods*. Piscataway, NJ, USA: IEEE Press, 1993. [Online]. Available: <https://ieeexplore.ieee.org/book/5264934>
- [22] C. A. Balanis, *Advanced Engineering Electromagnetics*. Hoboken, NJ, USA: Wiley, 2012.
- [23] J. Nocedal and S. J. Wright, *Numerical Optimization*, 2nd ed., ser. Springer Series in Operations Research and Financial Engineering. New York, NY, USA: Springer, 2006. [Online]. Available: <https://link.springer.com/book/10.1007/978-0-387-40065-5>